Research Article

ADVANCED PHOTONICS

Versatile cascade migrating photon avalanches for full-spectrum extremely nonlinear emissions and super-resolution microscopy

Hui Wu,[a,†] Binxiong Pan,[a,†] Qi Zhao,[a,†] Chenyi Wang,[a] Rui Pu,[a] Chang Liu,[a] Zeheng Chen,[a] Zewei Luo,[b] Jing Huang,[a] Wei Wei,[b] Tongsheng Chen,[b] and Qiuqiang Zhan[a,c,*]

[a]South China Normal University, South China Academy of Advanced Optoelectronics, Centre for Optical and Electromagnetic Research, Guangzhou, China

[b]South China Normal University, College of Biophotonics, MOE Key Laboratory & Guangdong Provincial Key Laboratory of Laser Life Science, Guangzhou, China

[c]South China Normal University, Guangdong Engineering Research Centre of Optoelectronic Intelligent Information Perception, Guangzhou, China

Abstract. Photon avalanche occurring in lanthanide-doped materials exhibits a giant optical nonlinear response of the emission intensity to the excitation intensity, which holds great potential in the applications of optical sensing, super-resolution imaging, quantum detection, and other techniques. However, strategies for developing photon avalanches in nanoparticles are limited, and many widely used lanthanide ions have not yet been able to generate high-efficiency avalanching emissions. A general strategy named cascade migrating photon avalanche was proposed to achieve efficient avalanching emissions with huge optical nonlinearities from a large number of emitters at the nanoscale and at room temperature. Specifically, the optical nonlinearity order of bright avalanched Tm^{3+}-emission was achieved at 63rd order by utilizing the Yb^{3+}/Pr^{3+}-codoped nano-engine. By further incorporating a Gd^{3+} sublattice migrating network, its avalanching energy can propagate over a long distance to arouse avalanching emission with extreme optical nonlinearities up to 45th order among various emitters (Tb^{3+}, Eu^{3+}, Dy^{3+}, Sm^{3+}) in multilayered nanostructures. By achieving abundant avalanching full-spectrum emissions, it would be highly conducive to applications in various fields. For instance, our strategy demonstrated its applicability in multi-color super-resolution microscopic imaging with single-nanoparticle sensitivity and resolution up to 48 nm, utilizing a single low-power 852 nm excitation beam.

Keywords: photon avalanches; super-resolution microscopy; upconversion luminescence; nonlinear microscopy.

Received Feb. 8, 2024; revised manuscript received Apr. 22, 2024; accepted for publication Aug. 15, 2024; published online Sep. 18, 2024.

[DOI: 10.1117/1.AP.6.5.056010]

1 Introduction

Photon avalanche (PA) is a unique upconversion mechanism exhibiting a giant optical nonlinear response,[1–3] which promises applications in advanced technologies such as microlasers,[4] integrated photonic circuits,[5] super-resolution microscopy,[6,7] optical sensing,[8,9] and quantum optics.[10] Unlike traditional upconversion processes[11] and avalanche-like mechanisms,[12] the crucial trick to realize the PA effect is to incorporate a non-resonant ground state absorption (GSA) process with a much stronger (usually 10^4 times) excited state absorption (ESA) process and maintain an efficient cross relaxation. In other words, an effective looping cycle should be kept to ensure the accumulation of electrons in the intermediate excited states, eventually leading to a burst of emission intensity. Due to the harsh excitation and energy transfer requirements, along with unignorable surface quenching in

*Address all correspondence to Qiuqiang Zhan, zhanqiuqiang@m.scnu.edu.cn

†These authors contributed equally to this work.

nanoparticles, the PA effect has long been restricted only in bulk materials.[13–20]

Recently, efficient PA phenomena have been reported separately in Tm^{3+}-doped and Yb^{3+}/Pr^{3+}-codoped nanoparticles by harnessing interionic energy transfer processes.[2,3] However, the PA effect achieved in the Tm^{3+} singly doped mechanism under 1064 nm excitation was only restricted to 800 nm emission.[2] Importantly, PA emissions with giant optical nonlinearity (≥ 20th order) have not yet been realized in many other ion systems. For example, lanthanide ions such as Tb^{3+}, Eu^{3+}, Dy^{3+}, and Sm^{3+}, which are widely used in many fields such as quantum cutting and lighting, cannot efficiently generate PA.[21] The unfavorable energy-looping-free characteristics of those energy levels are contrary to the prerequisites of triggering an efficient PA effect, making it challenging to find a proper PA excitation scheme (see Fig. S1 in the Supplementary Material). Although the PA effect can appear in some of these ions, the observed nonlinearities are relatively low, and single-nanoparticle brightness cannot be detected.[22] Therefore, developing a bright, huge-nonlinearity, universal mechanism with relevance to practice for generating PA emissions in various emitters and realizing advanced photonics applications remains a formidable task.

2 Results

2.1 Conceptualization and Theoretical Study of the Cascade Migrating Photon Avalanche Mechanism

In a three-level PA scheme based on a traditional single-type-ion strategy [Fig. 1(a)], the electrons at the ground state are first promoted to the metastable state through non-resonant GSA and followed by the higher-energy excited state to be populated via the resonant ESA. When the excitation intensity exceeds a critical threshold, the ESA and cross-relaxation process constitute a positive energy-looping cycle, boosting the population of the emitting levels and leading to a sharp emission burst. To achieve a high-efficiency PA effect in nanosized materials, a strategy of dual-type-ion doping was proposed to address issues such as large energy loss related to nonradiative relaxation, surface (-coupled concentration) quenching in nanomaterials [Fig. 1(a)]. This dual-type-ion (Yb^{3+}/Pr^{3+}) PA mechanism proposed in our previous work can also obtain Yb^{3+} sensitizer sublattices avalanched and thereby propagate the PA energy to different sites.[3] However, the challenge of these existing single/dual-type-ion PA mechanisms in extending the PA effect has been met with limited success, i.e., Ho^{3+} and Tm^{3+} ions only. Some important emitters with a large gap between the ground

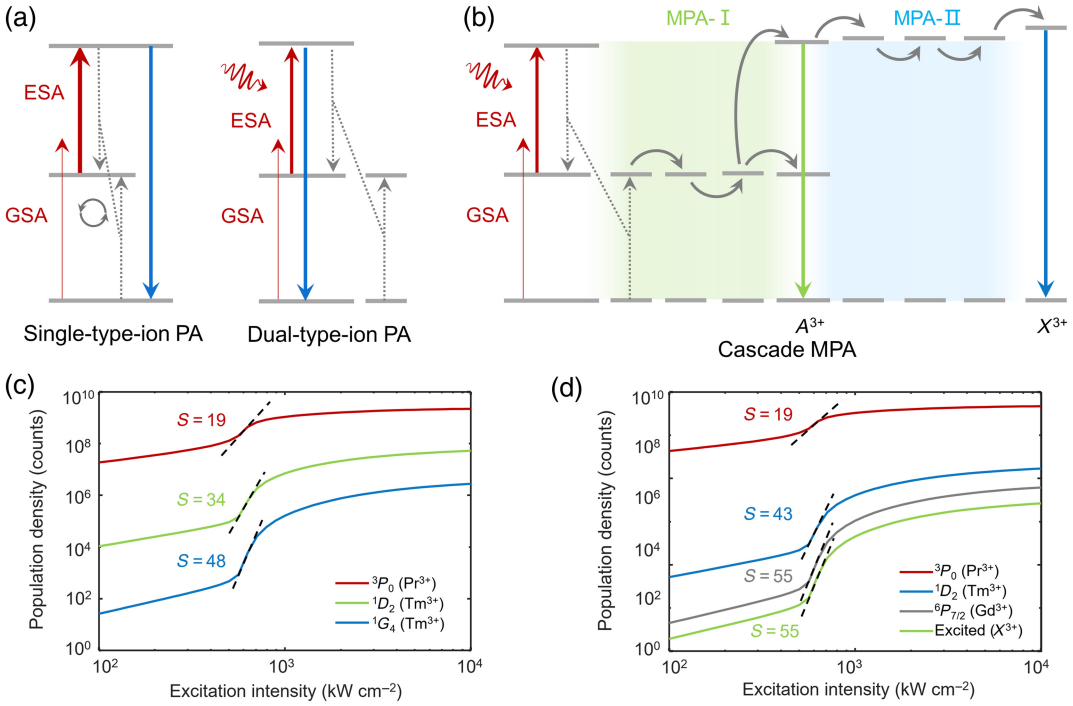

Fig. 1 Mechanistic diagram and theoretical simulations of cascade migrating photon avalanches (cMPA). (a) Two main kinds of existing PA strategies in the lanthanide-doped nanoparticles: single-type-ion and dual-type-ion. When the excitation intensity I exceeds the PA threshold I_{th}, the population in the metastable state grows rapidly due to cross-relaxation, leading to the occurrence of photon avalanches. (b) The proposed cMPA mechanism. With the synergetic effect of two migrating photon avalanche networks (MPA-I and MPA-II), the X^{3+} can get avalanched by establishing a cascade photon avalanche migration network for further energy transfer processes from A^{3+} to X^{3+}. (c) The simulation results of emission intensity versus excitation intensity curves at 484 nm (Pr^{3+}), 475 nm (Tm^{3+}), and 452 nm (Tm^{3+}) in the $Yb^{3+}/Pr^{3+}/Tm^{3+}$-codoped nanoparticles, featuring an S-shaped curve with a clear threshold. (d) The simulation plots of emission intensity versus excitation intensity show the amplified nonlinear response of X^{3+} through Yb^{3+} and Gd^{3+} cascade avalanching energy migration network.

state and the emitting states such as Tb^{3+}, Eu^{3+}, Dy^{3+}, and Sm^{3+} can hardly get avalanched likewise because the cooperative sensitization upconversion (CSU) process between the sensitizers Yb^{3+} and these ions is inefficient,[11] which hinders multiplexing capability and extremely nonlinear applications. Here, we proposed a powerful strategy named cascade migration photon avalanche (cMPA) to enrich the library of PA-achievable emitters. In this cMPA mechanism, A^{3+} collects the PA energy from the nano-engine in the first MPA network (MPA-I). Subsequently, it acts as the nano-engine of the secondary sublattice energy network (MPA-II), and the PA energy can further migrate to other emitters X^{3+} [Fig. 1(b)]. In other words, A^{3+} is a crucial accumulator in this cMPA mechanism to bridge the MPA-I and the MPA-II networks. For the proof of concept, we selected a Yb^{3+}/Pr^{3+}-codoped core as the PA nano-engine of MPA-I to establish the cMPA system. Tm^{3+} ion was chosen as the accumulator because it is capable of accepting PA energy from the MPA-I network via the Yb^{3+} sublattice and further incorporation with Gd^{3+} sublattice,[11] which can provide energy for a variety of ions that cannot be easily excited by Yb^{3+} sublattice. Therefore, the Tm^{3+}/Gd^{3+} network was designed as an MPA-II network for the cMPA system.

To demonstrate the feasibility of the above-designed cMPA mechanism, two theoretical models of cMPA were established based on differential rate equations, from which simulations and analysis were conducted. We first studied the $Yb^{3+}/Pr^{3+}/Tm^{3+}$-codoped nano-engine for the cMPA system (see Method S1 and Table S1 in the Supplementary Material). According to the calculations, clear excitation thresholds (420 kW cm^{-2}) and S-shaped curves of excitation-dependent population rates of the emitting states could be observed for the $Yb^{3+}/Pr^{3+}/Tm^{3+}$-codoped system [Fig. 1(c) and Fig. S2 in the Supplementary Material]. The obtained optical nonlinearities of Pr^{3+} emission at 484 nm and Tm^{3+} emissions at 475 nm and 452 nm were 19th order, 34th order, and 48th order, respectively. Under the excitation of the 852 nm laser, an efficient PA effect can be initiated in the Yb^{3+}/Pr^{3+}-doped core, then the avalanching energy migrates to the Tm^{3+}-doped shell through the Yb^{3+} sublattice network. Since the 475/452 nm emissions of Tm^{3+} correspond to three-/four-photon upconversion, the optical nonlinearities of the two emissions can be further amplified but showed a discrepancy in the amplification factor. Next, the whole cMPA system of $Yb^{3+}/Pr^{3+}/Tm^{3+}/Gd^{+}/X^{3+}$-codoped nanoparticles was theoretically modeled and studied (see Appendix A and Table S1 in the Supplementary Material). It was found that the cascade MPA networks enable the energy transfer from the $^6P_{7/2}$ state of Gd^{3+} ions to other well-matched emitters and finally arouse PA from them. Intriguingly, a positive PA evolution with optical nonlinearity being enhanced can be observed during the energy transfer from Tm^{3+} ions to Gd^{3+} ions, allowing cMPA to further amplify the optical nonlinear response [Fig. 1(d) and Fig. S3 in the Supplementary Material]. In this context, the group of emitters Tb^{3+}, Eu^{3+}, Dy^{3+}, and Sm^{3+} can all get avalanched under a fixed excitation scheme, driving extremely nonlinear applications and multiplexing capability.

2.2 Establishing a High-Efficiency Avalanche Engine for the cMPA System

Subsequently, experimental studies were carried out under the guidance of the aforementioned theory. To ensure the PA energy migrating to the Gd^{3+}-mediated network for achieving effective cMPA, the PA effect of Tm^{3+} ions is very crucial and has to be optimized in terms of emission intensity and optical nonlinearity [Fig. 2(a)]. We synthesized multilayered core-shell nanoparticles by controlling the Yb^{3+} doping concentrations $NaYF_4$:Yb/Pr$(x/0.5\%)$@$NaYF_4$:Yb/Tm$(y/4\%)$@$NaYF_4$:Yb/Pr$(x/0.5\%)$@$NaYF_4$ ($x = 15\%, 25\%$; $y = 3\%, 10\%$). The nanoparticles were synthesized according to our previously reported protocol[23] (see Method S2 in the Supplementary Material), which were characterized by transmission electron microscopy (see Fig. S4 in the Supplementary Material). A lab-built microspectroscope was utilized to characterize the PA effect (see Appendix B and Fig. S5 in the Supplementary Material). Under the 852 nm continuous-wave (CW) excitation, multicolor emissions from the $Yb^{3+}/Pr^{3+}/Tm^{3+}$ system were obtained, assigned to the transitions of $^3P_0 \rightarrow {}^3F_2$ (642 nm), $^1D_2 \rightarrow {}^3H_4$ (609 nm), $^3P_0 \rightarrow {}^3H_6$ (605 nm), $^3P_1 \rightarrow {}^3H_5$ (525 nm), $^3P_0 \rightarrow {}^3H_4$ (484 nm), and $^1D_2 \rightarrow {}^3F_4$ (452 nm) [Fig. 2(b)]. When appropriately increasing the Yb^{3+} concentration in the cascade shell (Yb^{3+}/Tm^{3+}) from 3% to 10%, the emission intensity of Tm^{3+} emitters at 452 nm was significantly enhanced. However, the 10% doping concentration of Yb^{3+} ions in the shell was close to the 15% Yb^{3+} doped in the PA core, resulting in a significant energy leakage for the core and weakening its PA optical nonlinearity. Therefore, the Yb^{3+} doping concentration in the avalanched Yb^{3+}/Pr^{3+}-codoped core was elevated from 15% to 25% accordingly. As the excitation-intensity-dependent emission curves shown in Fig. 2(c), a maximum optical nonlinearity order of 63.3 (62.3 ± 0.8 from three independent measurements, Fig. S6 in the Supplementary Material) was obtained when the Yb^{3+} concentrations in the core and shell layer were 25% and 10%, respectively. In our experiments, the excitation-emission power dependences were measured from nanoparticle ensembles. Therefore, optimizing the doping concentration can facilitate to establish highly efficient energy migrating pathways, enabling bright PA emission from Tm^{3+} ions with ultrahigh nonlinearity order [Fig. 2(d)].

2.3 Observing 43rd-Order Nonlinear Emission from Terbium Enabled by cMPA

To verify the possibility of energy transfer in the Gd^{3+}-based MPA-II network, we designed and fabricated multilayered nanoparticles with composites of $NaYF_4$:Yb/Pr(25%/0.5%)@$NaGdF_4$:Yb/Tm(10%/4%)@$NaGdF_4$:Tb(20%)@$NaYF_4$, as shown in Fig. 3(a).[24–26] High-angle annular dark-field scanning transmission electron microscopy (HADDF-STEM) and energy dispersive spectroscopy (EDS) mapping images confirmed the formation of the heterogeneous multilayered core-shell structures with clear component boundaries (see Fig. S7 in the Supplementary Material). As shown in the mechanistic diagram [Fig. 3(b)], the entire cMPA process for Tb^{3+} emission can be explained as below. The Yb^{3+}/Pr^{3+}-codoped core, as the role of the PA nano-engine, was first illuminated, and a huge optical nonlinear response was activated for both Pr^{3+} and Yb^{3+} ions. Next, the energy states of the Tm^{3+} ion, including the high-lying state $^1I_6$, were populated and thereby got avalanched by a five-step upconversion process from the Yb^{3+} sublattice. The avalanched behavior can rapidly propagate within and beyond the MPA-I network and then arrive in the MPA-II network via the energy transfer from the $^1I_6$ state (Tm^{3+}) to the $^6P_{7/2}$ state (Gd^{3+}). Finally, the avalanched Gd^{3+} network can easily pump

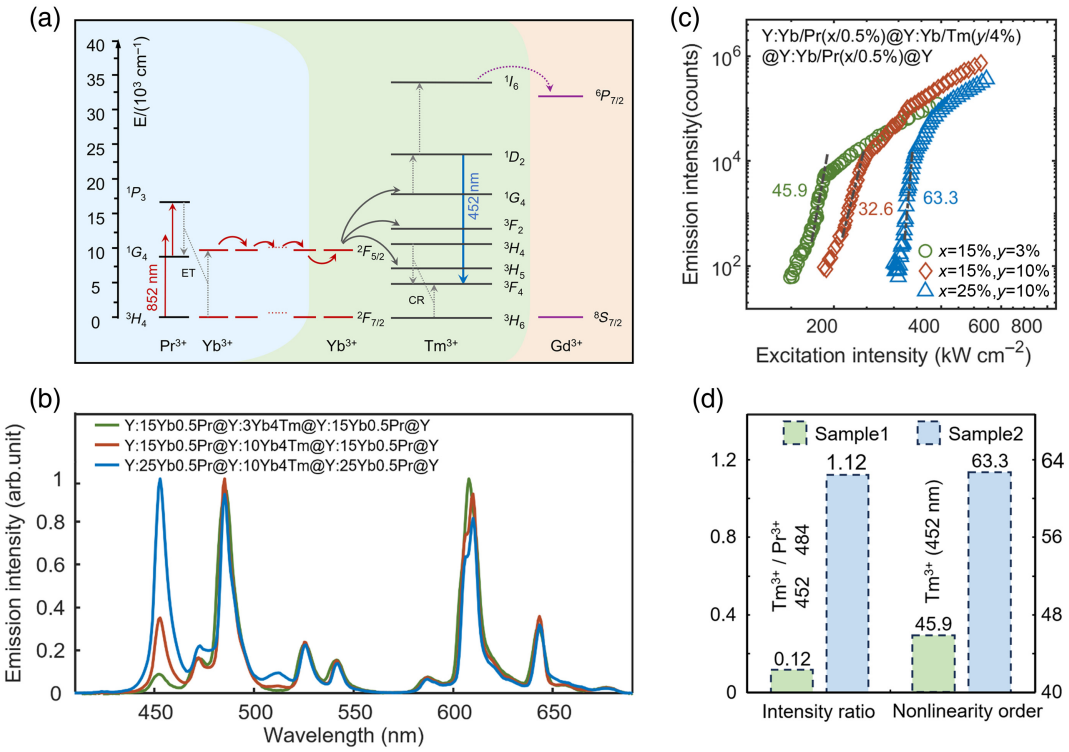

Fig. 2 PA effect of $Yb^{3+}/Pr^{3+}/Tm^{3+}$ nanoparticles. (a) The energy transfer mechanism of $Yb^{3+}/Pr^{3+}/Tm^{3+}$ system. (b) The luminescence spectra of the nanoparticles $NaYF_4$:Yb/Pr(x/0.5%)@$NaYF_4$:Yb/Tm (y/4%)@$NaYF_4$:Yb/ Pr(x/0.5%)@$NaYF_4$ (x = 15%, 25%; y = 3%, 10%), respectively, showing different intensities of Tm^{3+} under 452 nm emission while varying the Yb^{3+} concentration. (c) The experimental curves of Tm^{3+} 452 nm emission intensity versus excitation intensity for different nanoparticles with different Yb^{3+} concentrations. The nonlinearity order is derived from a linear fit of the log–log plot. (d) The comparisons of intensity ratio of Tm^{3+} (452 nm) emission intensity to Pr^{3+} (484 nm) and nonlinearity order from two samples [sample 1: $NaYF_4$:Yb/ Pr(15%/0.5%)@$NaYF_4$:Yb/Tm(3%/4%)@$NaYF_4$:Yb/ Pr(15%/0.5%)@$NaYF_4$ and sample 2: $NaYF_4$:Yb/ Pr(25%/0.5%)@$NaYF_4$:Yb/Tm(10%/4%)@$NaYF_4$:Yb/Pr(25%/0.5%) @ $NaYF_4$].

the emitting states of Tb^{3+} ions and enable multi-color PA emissions including 544 nm ($^5D_4 \rightarrow {}^7F_5$), 585 nm ($^5D_4 \rightarrow {}^7F_4$), and 620 nm ($^5D_4 \rightarrow {}^7F_3$). In the experiment, three characteristic emissions of Tb^{3+} ions at 544 nm, 585 nm, and 620 nm were obviously observed from the Tb^{3+}-doped PA nanoparticles under 852 nm excitation [Fig. 3(c)], which demonstrated the ability of the cMPA mechanism for propagating the PA effect to Tb^{3+} ions through the cascaded migration networks of Yb^{3+} and Gd^{3+} sublattice. The emission spectra of Tb^{3+} emitters under different excitation intensities were recorded, and the excitation-emission power dependence exhibited a typical S-shaped curve with a giant optical nonlinearity up to 42.6 (43.6 ± 0.9) order and a PA threshold at 370 kW cm^{-2} [Fig. 3(d)]. The nonlinearity order for 484 nm emission of Pr^{3+} emitters was 25.7, while it was 36.6 for Tm^{3+} 452 nm emission. The multi-photon upconversion process within the MPA-I network further amplified the nonlinearity of the PA engine, resulting in the nonlinearity enabled by the cMPA mechanism far exceeding that by the Tm^{3+} singly doped PA mechanism.[22] To further confirm that the PA energy of Tb^{3+} emitters originated from the Yb^{3+}/Pr^{3+}-codoped nano-engine, we also switched to 980 nm excitation for the nanoparticles and investigated the upconversion luminescence likewise. No obvious characteristic emission of Pr^{3+} ions was observed under 980 nm excitation [Fig. 3(e)]. In contrast, Tb^{3+} ions can be excited through the energy migration-mediated upconversion (EMU) process, exhibiting intense emissions. As expected, the inactivation of the PA engine core made the Tb^{3+} emissions unavalanched [Fig. 3(f)].

Theoretically, the avalanched Yb^{3+}/Pr^{3+}-codoped core can also alternatively arouse the PA effect on Tb^{3+} ions through the Yb^{3+}-mediated CSU process. We also fabricated Tb^{3+}-doped CSU nanoparticles and studied its PA properties [Fig. 3(g)]. It is well known that, in this case, the energy of a pair of excited Yb^{3+} has to be simultaneously transferred to one adjacent Tb^{3+} ion, meaning that the CSU process is a very inefficient, second-order cooperative sensitization process.[27] Under 852 nm excitation, the luminescent spectra of Tb^{3+}-doped CSU nanoparticles were measured, and they overlapped very well with that of Yb^{3+}/Pr^{3+}-codoped PA nanoparticles as shown in Fig. 3(h), indicating that no emission can be observed from Tb^{3+} ions. This verified that the proposed cMPA mechanism is indispensable as well as powerful to arouse PA emissions from Tb^{3+} ions.

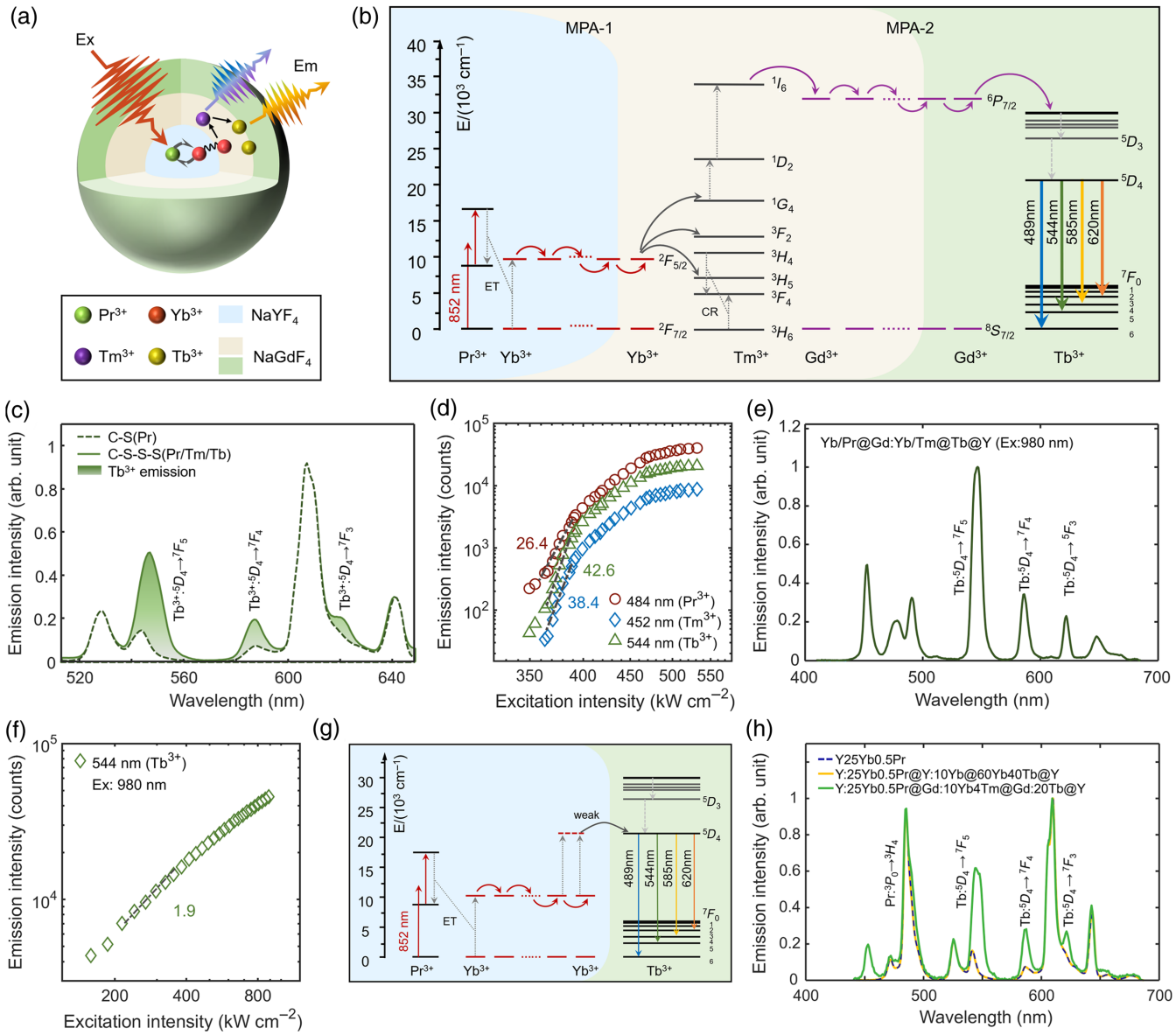

Fig. 3 PA effect in Tb^{3+}-doped nanoparticles realized by cMPA mechanism. (a) Schematic of the $Yb^{3+}/Pr^{3+}/Tm^{3+}/Tb^{3+}$ multi-layer nanostructure. (b) The energy transfer cMPA mechanism of Tb^{3+}-doped system. Through the Gd^{3+} sublattice network, the avalanching energy can be further transferred from Tm^{3+} to the Tb^{3+}. (c) The luminescence spectra of the nanoparticles $NaYF_4$:Yb/Pr(25%/0.5%)@$NaYF_4$ and $NaYF_4$:Yb/Pr(25%/0.5%)@$NaGdF_4$:Yb/Tm(10%/4%)@$NaGdF_4$:Tb(20%)@$NaYF_4$, indicating the Tb^{3+} characteristic emissions at 544 nm, 586 nm, and 620 nm. (d) The experimental curves of emission intensity versus excitation intensity for the nanoparticles $NaYF_4$:Yb/Pr(25%/0.5%)@$NaGdF_4$:Yb/Tm(10%/4%)@$NaGdF_4$:Tb(20%)@$NaYF_4$ under an 852 nm CW laser. The obtained optical nonlinearities of Pr^{3+} emission at 484 nm, Tm^{3+} emission at 452 nm, and Tb^{3+} emission at 544 nm were 26.4, 38.4, and 42.6 orders, respectively. The nonlinearity order is derived from a linear fit of the log–log plot. (e) The luminescence spectra of Tb^{3+}-doped cMPA nanoparticles under 980 nm excitation. (f) The experimental curve of emission intensity versus excitation intensity at 544 nm (Tb^{3+}) under 980 nm excitation. (g) Yb^{3+}-mediated CSU mechanism of Tb^{3+}-doped system. (h) Luminescent spectra of Yb^{3+}/Pr^{3+}-codoped PA nanoparticles [$NaYF_4$:Yb/Pr(25%/0.5%)], Tb^{3+}-doped CSU nanoparticles [$NaYF_4$:Yb/Pr(25%/0.5%)@$NaYF_4$:Yb(10%)@$NaYF_4$:Yb/Tb(60%/40%)@$NaYF_4$], and Tb^{3+}-doped cMPA nanoparticles [$NaYF_4$:Yb/Pr(25%/0.5%)@$NaGdF_4$:Yb/Tm(10%/4%)@$NaGdF_4$:Tb(20%)@$NaYF_4$].

2.4 Extending cMPA to Other Emitters for Full-Spectrum Extremely Nonlinear Emissions

To further extend PA behavior to many other emitters through the proposed cMPA mechanism, we synthesized Eu^{3+}-, Dy^{3+}-, and Sm^{3+}-activated four-layered core-shell nanoparticles, respectively, $NaYF_4:Yb/Pr(25\%/0.5\%)@NaGdF_4:Yb/Tm(10\%/4\%)@NaGdF_4:X@NaYF_4$ ($X = 20\%$ Eu, 5% Dy, or 5% Sm). As the ions Eu^{3+} and Dy^{3+} have a similar structure of intrinsic electronic energy states to the Tb^{3+} ion, they can capture the PA energy from the Gd^{3+}-based cMPA network [Figs. 4(a) and 4(d)]. Two characteristic emission bands from Eu^{3+} ions were observed with peaks at 592 nm ($^5D_0 \rightarrow {}^7F_1$) and 617 nm ($^5D_0 \rightarrow {}^7F_2$) [Fig. 4(b)], achieving a 45.3 (44.9 ± 2.2) order optical nonlinearity at the 592 nm emission when the laser power was approaching the PA threshold [~330 kW cm^{-2}, Fig. 4(c)]. Similarly, the characteristic emission peak of Dy^{3+} ions was observed at 574 nm ($^4F_{9/2} \rightarrow {}^6H_{11/2}$) with a giant optical nonlinearity up to 45.4 (44.7 ± 1.2) order [Figs. 4(e) and 4(f)]. The PA threshold of Dy^{3+}-doped cMPA nanoparticles was around 400 kW cm^{-2}. The variation in their PA thresholds may be attributed to the discrepancies of energy transfer efficiency among different ions, after all the ions with less pumping efficiency would require higher energy to get avalanched. Similar to the result of Tb^{3+} ions, here Eu^{3+} and Dy^{3+} ions did not exhibit any PA nature under 980 nm excitation (see Fig. S8 in the Supplementary Material). In the case of Sm^{3+}-doped nanoparticles, the energy transfer mechanism is analogous to that of Tb^{3+}, Eu^{3+}, and Dy^{3+} ions [see Fig. S9(a) in the Supplementary Material]. With the same cMPA mechanism, a certain PA emission can also be observed from Sm^{3+} ions at 563 nm ($^4G_{5/2} \rightarrow {}^6H_{5/2}$) [see Fig. S9(b) in the Supplementary Material], although its intensity was too weak to measure the excitation-intensity-dependent emission curve, which was mainly due to the largely enhanced non-radiative relaxation effect for Sm^{3+} ions with very dense energy states.[11] Overall, the developed cMPA mechanism can promote the full-spectrum PA emission from these lanthanide emitters, including but not limited to the visible light at 400 to 700 nm [Fig. 4(g)]. The Tm^{3+} singly doped PA mechanism under 1064 nm excitation can also enable avalanching emission from a series of lanthanide ions.[12] However, the energy looping locked the energy mainly to the $^3H_4$ state featuring an 800 nm PA emission, and the higher-lying energy states such as $^1I_6$ cannot be effectively populated, resulting in very weak emission and low optical nonlinearities from the acceptor ions (see Fig. S10 in the Supplementary Material).

2.5 Extremely Nonlinear cMPA Super-Resolution Microscopy

With the capability of generating the high-efficiency PA effects from many lanthanide ions, our proposed cMPA mechanism provides new insights into fascinating applications of relevance, i.e., super-resolution microscopic imaging.[28,29] As a demonstration, we implemented low-power, single-NIR-CW-beam optical nanoscopy. We built a laser-scanning microscope coupled with an 852 nm CW beam for cMPA super-resolution microscopy [Fig. 5(a), see Appendix B]. First, the Tm^{3+}-doped cMPA nanoparticles distributed on the slide were imaged. By adjusting the excitation intensity, a series of images at 605 nm of Pr^{3+} emitters [Fig. 5(b)] and at 452 nm of Tm^{3+} emitters [Fig. 5(c)] were obtained. In the 452 nm detection channel of Tm^{3+}, the diffraction-unlimited full width at half-maximum (FWHM) of the effective point spread function (PSF) was measured to be 48 nm ($\lambda/17$) at an excitation intensity of 320 kW cm^{-2} [Fig. 5(c-iv)]. In comparison, a diffraction-limited FWHM of 225 nm was observed at a high-power laser excitation of 1403 kW cm^{-2} [Fig. 5(c-ii)], demonstrating a five-fold improvement in the lateral resolution. It is worth mentioning that it would take time for the PA energy looping cycles to build up an efficient PA effect. In the scanning imaging experiments, we took a 100 μs pixel dwell time, compatible with a standard confocal microscope, and achieved super-resolution imaging at high speed.[30,31] The improvement of the imaging resolution reflected the obtained non-steady-state PA nonlinearity orders during imaging were slightly lower than the steady-state test results. In the 605 nm detection channel of Pr^{3+}, the lateral resolution was improved by three-fold [Figs. 5(b-ii) and 5(b-iv)]. These results confirmed that the lateral resolution was higher in the 452 nm channel, corroborating the higher nonlinearity order of PA in Tm^{3+} ions compared to Pr^{3+} ions. Tm^{3+} ions exhibited higher sensitivity to the variation of excitation intensity, thereby enabling clearer separation of two adjacent nanoparticles (separated by 200 nm) in the 452 nm channel [Figs. 5(b-v) and 5(c-v)]. To further verify the super-resolution imaging capability in X^{3+} (X = Tb/Eu/Dy), we took Tb^{3+} ions as an example and imaged Tb^{3+}-doped cMPA nanoparticles. A series of images at 484 nm of Pr^{3+} ions [Fig. 5(d)] and at 545 nm of Tb^{3+} ions [Fig. 5(e)] emission peaks were captured. By varying the excitation intensity, the images showed a diffraction-unlimited FWHM of 80 nm ($\lambda/10$) in the 545 nm detection channel [Fig. 5(e-iv)]. Compared with the diffraction-limited FWHM of 238 nm [Fig. 5(e-ii)], the lateral resolution was improved by three-fold. Similarly, the resolution improvement of the Tb^{3+} channel is more significant than that of the Pr^{3+} channel [Fig. 5(d-iv)], which is consistent with the observed excitation power-dependent curves. These results further confirm that the PA energy can be effectively transferred to the activator ions in the shell layer through the proposed cMPA mechanism, enabling long-distance PA energy transfer pathways that hold promise for the applications of many other ions in super-resolution microscopy.

In addition, taking advantage of the full-spectrum and tunable threshold properties of cMPA emissions, we demonstrated multi-color cMPA super-resolution microscopy using a single excitation beam [Fig. 6(a)]. The Yb^{3+}/Pr^{3+}-codoped PA nanoparticles and the Tb^{3+}-doped cMPA nanoparticles were mixed and evenly dispersed on the coverslip for multi-color super-resolution imaging. Interestingly, cMPA nanoprobes with different PA thresholds provided a new dimension of excitation-power-controlled multiplexing imaging. The PA threshold of Yb^{3+}/Pr^{3+}-codoped PA nanoparticles (~70 kW cm^{-2}) is lower than that of the Tb^{3+}-doped cMPA nanoparticles (~370 kW cm^{-2}). By adjusting the excitation power, we could selectively detect emissions from different nanoparticles [Figs. 6(b)–6(d)]. We have experimentally demonstrated that our full-spectrum cMPA mechanism can be used for dual-color super-resolution microscopic imaging [Figs. 6(e) and 6(f)]. Furthermore, the cMPA nanoparticles do not exhibit photobleaching or photodarkening (see Fig. S11 in the Supplementary Material), providing high-efficiency emission and excellent photostability during long-term laser-scanning imaging and monitoring.

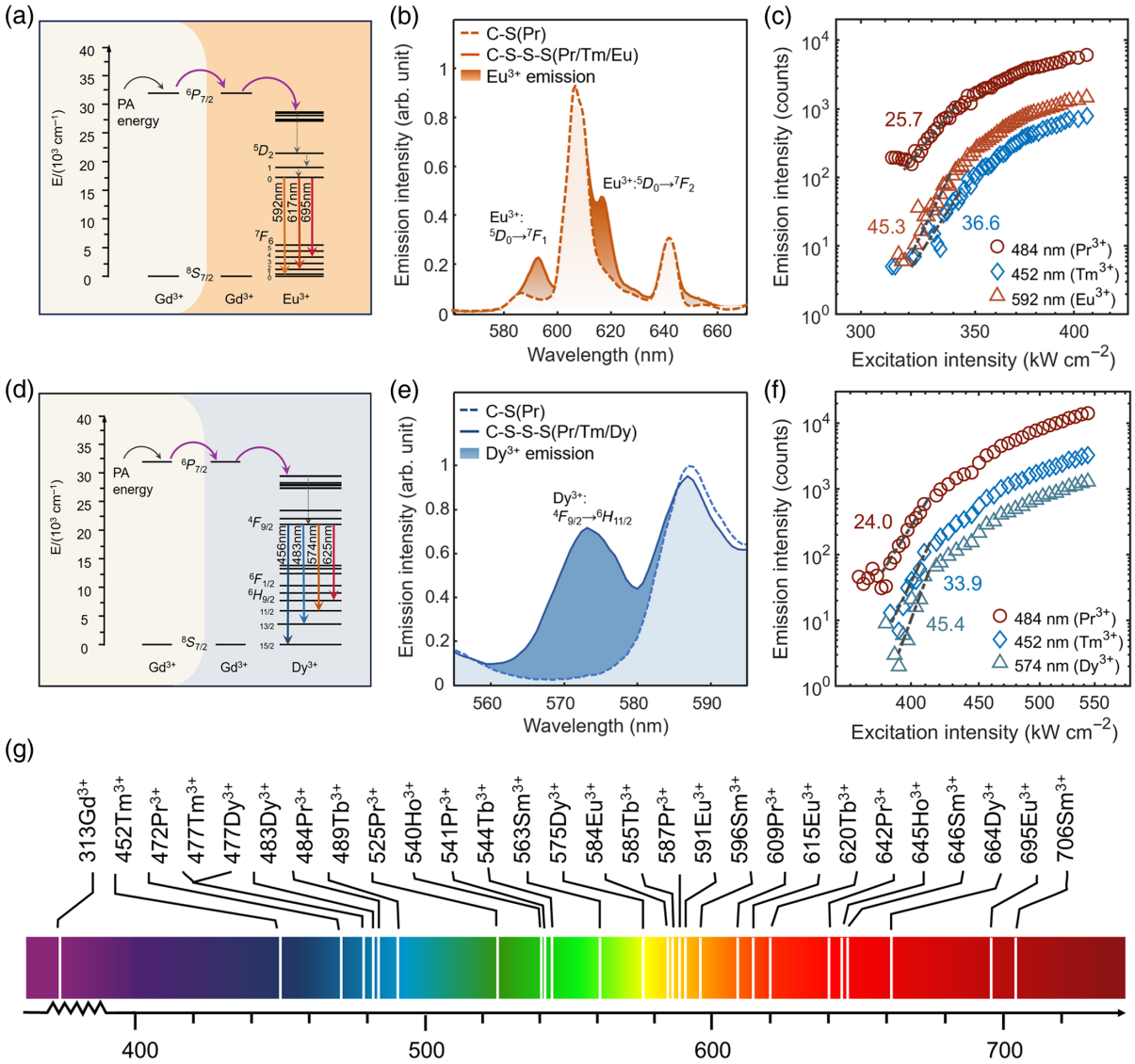

Fig. 4 Full-spectrum extremely nonlinear PA emissions enabled by cMPA mechanism. (a) The cMPA mechanism for Eu^{3+}-doped system. (b) The luminescence spectra of the nanoparticles $NaYF_4$:Yb/Pr(25%/0.5%)@$NaYF_4$ and $NaYF_4$:Yb/Pr(25%/0.5%)@$NaGdF_4$:Yb/Tm(10%/4%)@$NaGdF_4$:Eu(20%)@$NaYF_4$, respectively. The characteristic emissions of Eu^{3+} exist at 592 nm and 617 nm. (c) The experimental curves of emission intensity versus excitation intensity for the Eu^{3+}-doped nanoparticles under 852 nm excitation. The obtained optical nonlinearities of Pr^{3+} emission at 484 nm, Tm^{3+} emission at 452 nm, and Eu^{3+} emission at 592 nm were 25.7, 36.6, and 45.3 orders, respectively. The nonlinearity order is derived from a linear fit of the log–log plot. (d) The cMPA mechanism for Dy^{3+}-doped system. (e) The luminescence spectra of the nanoparticles $NaYF_4$:Yb/Pr(25%/0.5%)@$NaYF_4$ and $NaYF_4$:Yb/Pr(25%/0.5%)@$NaGdF_4$:Yb/Tm(10%/4%) @ $NaGdF_4$:Dy(5%)@$NaYF_4$, respectively. The characteristic emission of Dy^{3+} exists at 574 nm. (f) The experimental curves of emission intensity versus excitation intensity for the Dy^{3+}-doped nanoparticles under 852 nm excitation. The obtained optical nonlinearities of Pr^{3+} emission at 484 nm, Tm^{3+} emission at 452 nm, and Dy^{3+} emission at 574 nm were 24.0, 33.9, and 45.4 orders, respectively. The nonlinearity order is derived from a linear fit of the log–log plot. (g) Emission peaks of lanthanide ions capable of photon avalanche with extremely nonlinear response, showing a full-spectrum PA range through the cMPA mechanism.

3 Discussion and Conclusion

By cooperating with the Gd^{3+} and Yb^{3+} sublattice networks in a multilayered core-shell structure, we have successfully developed a universal mechanism that can generate abundant energy transfer paths, leading to full-spectrum PA with ultrahigh nonlinearities (45th and 63rd order). Through elaborate design and control of this cMPA mechanism, different emitters with mismatched energy states against the PA rules can be activated for an extremely optical nonlinear response. By optimizing

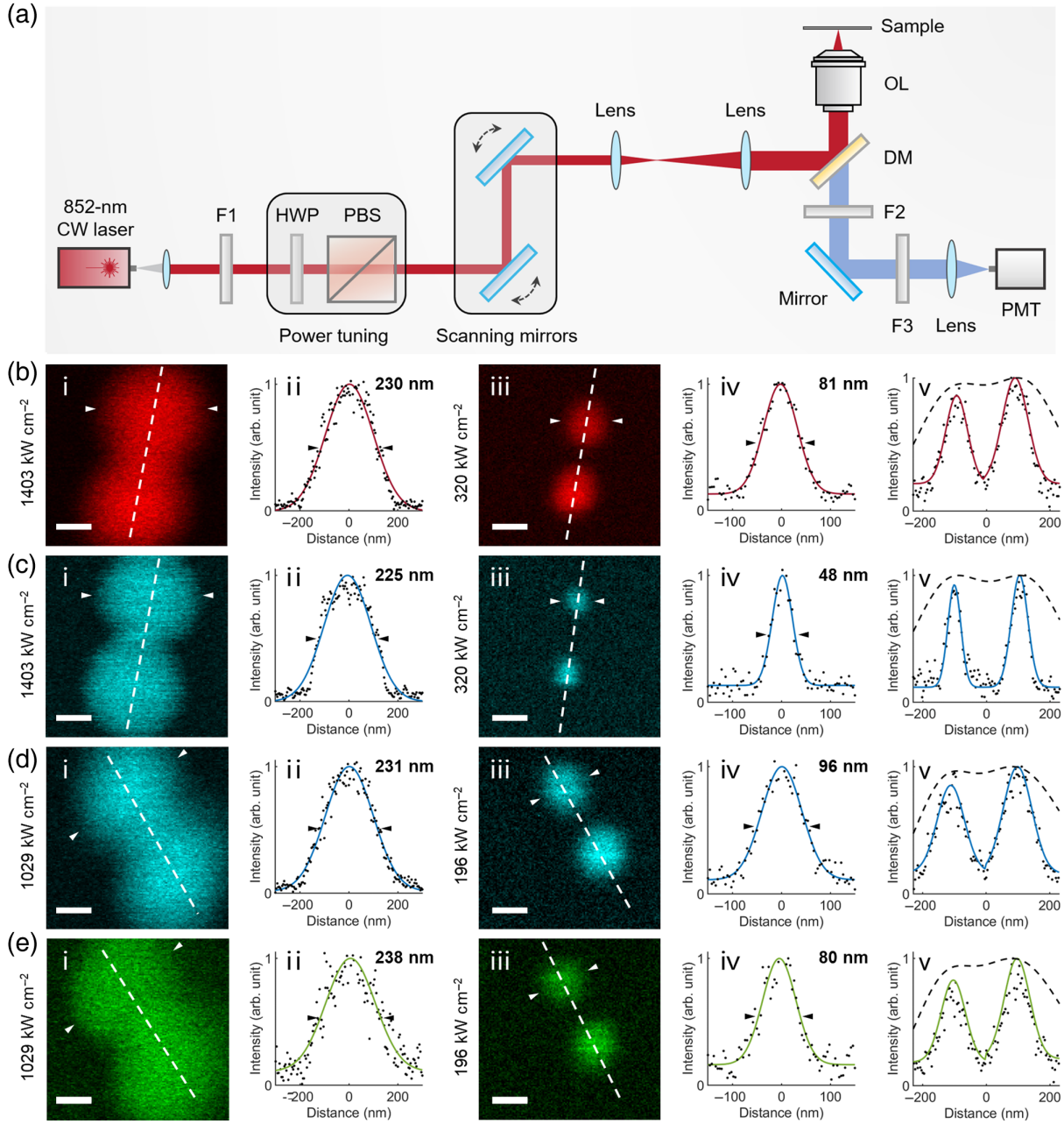

Fig. 5 Extremely nonlinear cMPA super-resolution microscopic imaging. (a) The cMPA nanoscopy system with a low-power, single-CW beam is compatible with the standard multiphoton/confocal laser scanning microscope. OL, 100× NA = 1.45 oil-immersed objective lens; PMT, photomultiplier tube; DM, 690 nm short-pass dichroic mirror; F1, 850/10 nm band-pass filter; F2, 694 nm short-pass filter; F3, 665 nm short-pass filter; PBS, polarizing beam splitter; HWP, half-wave plate. (b-i), (c-i) Single-nanoparticle of $NaYF_4$:Yb/ Pr(25%/0.5%)@$NaYF_4$:Yb/Tm(10%/4%)@$NaYF_4$:Yb/ Pr(25%/0.5%)@$NaYF_4$ imaged at 605 nm of Pr^{3+} (red) and at 452 nm of Tm^{3+} (blue) emission peak, excited by an 852 nm Gaussian beam with 1403 kW cm^{-2}. (b-iii), (c-iii) Super-resolution imaging of panels (b-i) and (c-i), excited near the PA threshold (320 kW cm^{-2}). (b-ii), (b-iv) Line profile analyses of single nanoparticles indicated by white arrows in panels (b-i) and (b-iii), showing a PSF FWHM of 230 nm and 81 nm, respectively. (c-ii), (c-iv) Line profile analyses of single nanoparticles indicated by the white arrow in panels (c-i) and (c-iii), showing a PSF FWHM of 225 nm and 48 nm, respectively. (b-v) Line profile analysis (black) of a line cut from (b-i), compared with another line cut through a super-resolution image (red) in panel (b-iii). (c-v) As in panel (b-v), but for the image of Tm^{3+} (452 nm) emission peak. (d-i), (e-i) Single-nanoparticle of $NaYF_4$:Yb/ Pr(25%/0.5%)@$NaGdF_4$:Yb/Tm(10%/4%)@$NaGdF_4$:Tb(20%)@$NaYF_4$ imaged at 484 nm of Pr^{3+} (blue) and at 545 nm of Tb^{3+} (green) emission peak, excited by

Fig. 5 (*Continued*) an 852 nm Gaussian beam with 1029 kW cm^{-2}. (d-iii), (e-iii) Super-resolution imaging of panels (d-i) and (e-i), excited near the PA threshold (196 kW cm^{-2}). (d-ii), (d-iv) Line profile analyses of single nanoparticles indicated by a white arrow in panels (d-i) and (d-iii), showing a PSF FWHM of 231 nm and 96 nm, respectively. (e-ii), (e-iv) Line profile analyses of single nanoparticles indicated by white arrow in panels (e-i) and (e-iii), showing a PSF FWHM of 238 nm and 80 nm, respectively. (d-v) Line profile analysis (black) of a line cut from (d-i), compared with another line cut through a super-resolution image (blue) in panel (d-iii). (e-v) As in panel (d-v), but for the image of Tb^{3+} (545 nm) emission peak. Scale bars are 100 nm, and the pixel dwell time is 100 μs.

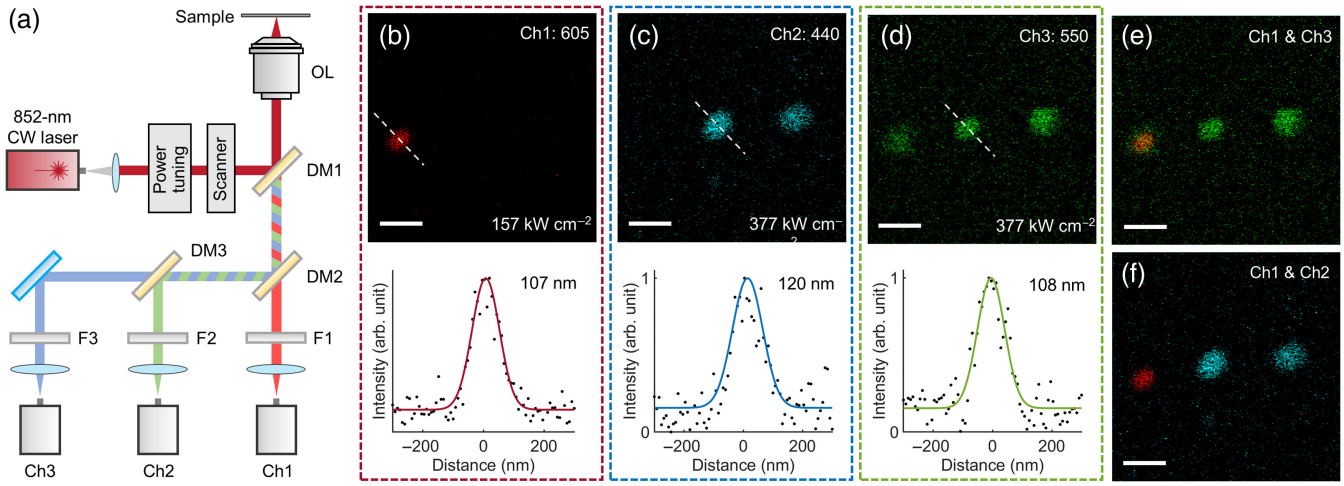

Fig. 6 Single-beam multi-color cMPA super-resolution microscopy. (a) The schematic diagram of the cMPA nanoscopy system. OL, 100× NA = 1.45 oil-immersed objective lens; DM1, 690 nm short-pass dichroic mirror; DM2, 593 nm short-pass dichroic mirror; DM3, 458 nm short-pass dichroic mirror; F1, 605/30 nm band-pass filter; F2, 550/20 nm band-pass filter; F3, 440/40 nm band-pass filter. (b) Channel 1: 605 nm band for the nanoparticles $NaYF_4$:Yb/ Pr(15%/0.5%)@ $NaYF_4$. The line profile showed Pr^{3+} with a resolution of 107 nm at 157 kW cm^{-2} excitation. (c) Channel 2: 452 nm band for the nanoparticles $NaYF_4$:Yb/ Pr(25%/0.5%)@$NaGdF_4$: Yb/Tm(10%/4%)@$NaGdF_4$:Tb(20%)@$NaYF_4$. The line profile showed Tm^{3+} with a resolution of 120 nm at 377 kW cm^{-2} excitation. (d) Channel 3: 544 nm band for the nanoparticles $NaYF_4$:Yb/ Pr(25%/0.5%)@$NaGdF_4$:Yb/Tm(10%/4%)@$NaGdF_4$:Tb(20%)@$NaYF_4$. The line profile showed Tb^{3+} with a resolution of 108 nm at 377 kW cm^{-2} excitation. (e) Dual-color super-resolution imaging of red and green luminescence from the above two nanoprobes. (f) Dual-color super-resolution imaging of red and blue luminescence from the above two nanoprobes. Scale bars are 300 nm, and the pixel dwell time is 100 μs.

the Yb^{3+}/Pr^{3+}-codoped nano-engine, we observed a bright 452 nm emission of Tm^{3+} with a giant optical nonlinearity of 63rd order. Via the cMPA strategy, other spatially separated ions (Tb^{3+}, Eu^{3+}, Dy^{3+}, Sm^{3+}) can be activated by this optimized interior PA engine, largely enriching the spectral range of PA emission not limited to the visible range. The observed optical nonlinearity up to 45th order and the achieved bright single-nanoparticle imaging verify that cMPA is a very efficient and powerful PA mechanism of practical significance. As an example, we realized sub-50-nm single-beam super-resolution imaging with the advantages of single-nanoparticle sensitivity and non-photobleaching. With the cMPA concept, we also proposed excitation power as a new dimension for multiplexing and demonstrated dual-color super-resolution imaging. The inherited full-spectrum nonlinear emissions are capable of multiphoton microscopy with single-beam shaping and imaging adaptive optics. In addition, the demonstrated cMPA might also be extended to other luminophores, such as inorganic-organic hybrid luminescence systems, to generate significant optical nonlinearities from them.[32] We envision that the cMPA capabilities will provide new insights into designing next-generation nonlinear nanomaterials with significant optical nonlinearity, enabling cutting-edge applications such as low-power single-beam-driven diffraction-unlimited sensing,[2] miniaturized lasers,[4] optical data storage,[33,34] and lithography.[35]

4 Appendix A: Theoretical Modeling for the cMPA System

The photon avalanches of the system doped with Yb^{3+}/Pr^{3+}-Yb^{3+}/Tm^{3+}/Gd^{3+}-Gd^{3+}/X^{3+} can be described by a set of rate equations. The energy scheme and energy transfer pathway are shown in Fig. S3 of the Supplementary Material. The rate equations for each of the energy states can be established as follows:

$$\mathrm{Pr}^{3+}(^3H_4):\ \frac{\mathrm{d}n_0}{\mathrm{d}t} = -\frac{I_{852}}{\hbar\upsilon}\sigma_0 n_0 - w_1 n_{Yb1} n_0 + w_1' n_{Yb0} n_5 + \beta_1 n_1 + \frac{n_6}{\tau_6} + b_{70}\frac{n_7}{\tau_7} + b_{80}\frac{n_8}{\tau_8} - c_1 n_0 n_7 - c_5 n_0 n_7 - c_4 n_0 n_7 - c_3 n_0 n_5 - c_6 n_0 n_8 - c_2 n_0 n_6 - c_7 n_0 n_6, \tag{1}$$

$$\mathrm{Pr}^{3+}(^3H_5):\ \frac{\mathrm{d}n_1}{\mathrm{d}t} = -\beta_1 n_1 + \beta_2 n_2 + \frac{n_5}{\tau_5} + b_{71}\frac{n_7}{\tau_7} + b_{81}\frac{n_8}{\tau_8}, \tag{2}$$

$$\mathrm{Pr}^{3+}(^3H_6):\ \frac{\mathrm{d}n_2}{\mathrm{d}t} = -\beta_2 n_2 + \beta_3 n_3 + b_{82}\frac{n_8}{\tau_8} + c_5 n_0 n_7 + c_4 n_0 n_7 + c_3 n_0 n_5, \tag{3}$$

$$\mathrm{Pr}^{3+}(^3F_2):\ \frac{\mathrm{d}n_3}{\mathrm{d}t} = -\beta_3 n_3 + \beta_4 n_4 + b_{73}\frac{n_7}{\tau_7} + c_3 n_0 n_5, \tag{4}$$

$$\mathrm{Pr}^{3+}(^3F_4):\ \frac{\mathrm{d}n_4}{\mathrm{d}t} = -\beta_4 n_4 + \beta_5 n_5 + w_2 n_{Yb0} n_6 - w_2' n_{Yb1} n_4 + c_2 n_0 n_6 + c_7 n_0 n_6, \tag{5}$$

$$\mathrm{Pr}^{3+}(^1G_4):\ \frac{\mathrm{d}n_5}{\mathrm{d}t} = -\frac{I_{852}}{\hbar\upsilon}\sigma_5 n_5 + \frac{I_{852}}{\hbar\upsilon}\sigma_0 n_0 - \beta_5 n_5 + w_1 n_{Yb1} n_0 - w_1' n_{Yb0} n_5 + w_3 n_{Yb0} n_7 - w_3' n_{Yb1} n_5 - 2c_1 n_0 n_7 - c_3 n_0 n_5 + c_2 n_0 n_6 + c_7 n_0 n_6 - \frac{n_5}{\tau_5}, \tag{6}$$

$$\mathrm{Pr}^{3+}(^1D_2):\ \frac{\mathrm{d}n_6}{\mathrm{d}t} = -w_2 n_{Yb0} n_6 + w_2' n_{Yb1} n_4 - \frac{n_6}{\tau_6} + \beta_7 n_7 + c_5 n_0 n_7 + c_4 n_0 n_7 + c_6 n_0 n_8 - c_2 n_0 n_6 - c_7 n_0 n_6, \tag{7}$$

$$\mathrm{Pr}^{3+}(^3P_0):\ \frac{\mathrm{d}n_7}{\mathrm{d}t} = -w_3 n_{Yb0} n_7 + w_3' n_{Yb1} n_5 - \frac{n_7}{\tau_7} - \beta_7 n_7 + \beta_8 n_8 - c_1 n_0 n_7 - c_5 n_0 n_7 - c_4 n_0 n_7, \tag{8}$$

$$\mathrm{Pr}^{3+}(^3P_1):\ \frac{\mathrm{d}n_8}{\mathrm{d}t} = -\beta_8 n_8 + \frac{I_{852}}{\hbar\upsilon}\sigma_5 n_5 - \frac{n_8}{\tau_8} - c_6 n_0 n_8, \tag{9}$$

$$\mathrm{Yb_1}^{3+}(^2F_{7/2}):\ \frac{\mathrm{d}n_{Yb1}}{\mathrm{d}t} = -\frac{I_{852}}{\hbar\upsilon}\sigma_0 n_0 + \frac{n_{Yb1}}{\tau_{Yb}} + w_1 n_{Yb1} n_0 - w_1' n_{Yb0} n_5 - w_2 n_{Yb0} n_6 + w_2' n_{Yb1} n_4 - w_3 n_{Yb0} n_7 + w_3' n_{Yb1} n_5 - w_4 n_{Yb1} n_{Yb11}, \tag{10}$$

$$\mathrm{Yb_1^{3+}}(^2F_{5/2}):\ \frac{\mathrm{d}n_{Yb0}}{\mathrm{d}t} = \frac{I_{852}}{\hbar\upsilon}\sigma_0 n_0 - \frac{n_{Yb1}}{\tau_{Yb}} - w_1 n_{Yb1} n_0 + w_1' n_{Yb0} n_5 + w_2 n_{Yb0} n_6 - w_2' n_{Yb1} n_4 + w_3 n_{Yb0} n_7 - w_3' n_{Yb1} n_5 + w_4 n_{Yb1} n_{Yb11}, \tag{11}$$

$$\mathrm{Yb_2^{3+}}(^2F_{7/2}):\ \frac{\mathrm{d}n_{Yb11}}{\mathrm{d}t} = -\frac{I_{852}}{\hbar\upsilon}\sigma_0 n_0 + \frac{n_{Yb11}}{\tau_{Yb}} - w_5 n_{Yb11} n_9 - w_6 n_{Yb11} n_{10} - w_7 n_{Yb11} n_{12} - w_8 n_{Yb11} n_{14} - w_9 n_{Yb11} n_{15} + w_4 n_{Yb1} n_{Yb11}, \tag{12}$$

$$\mathrm{Yb_2^{3+}}(^2F_{5/2}):\ \frac{\mathrm{d}n_{Yb10}}{\mathrm{d}t} = \frac{I_{852}}{\hbar\upsilon}\sigma_0 n_0 n_0 - \frac{n_{Yb11}}{\tau_{Yb}} + w_5 n_{Yb11} n_9 + w_6 n_{Yb11} n_{10} + w_7 n_{Yb11} n_{12} + w_8 n_{Yb11} n_{14} + w_9 n_{Yb11} n_{15} - w_4 n_{Yb1} n_{Yb11}, \tag{13}$$

$$\mathrm{Tm}^{3+}(^3H_6):\ \frac{\mathrm{d}n_9}{\mathrm{d}t} = -w_5 n_{Yb11} n_9 + w_{10} n_{16} n_{17} + \frac{b_{912} n_{12}}{\tau_{12}} + \frac{b_{914} n_{14}}{\tau_{14}} + \frac{b_{915} n_{15}}{\tau_{15}} + \frac{n_{10}}{\tau_{10}} + \frac{n_{13}}{\tau_{13}} - c_{12} n_9 n_{15} - c_8 n_9 n_{12}, \tag{14}$$

$$\mathrm{Tm}^{3+}(^3F_4):\ \frac{\mathrm{d}n_{10}}{\mathrm{d}t} = -w_6 n_{Yb11} n_{10} - \frac{n_{10}}{\tau_{10}} + \frac{b_{1012} n_{12}}{\tau_{12}} + \frac{b_{1014} n_{14}}{\tau_{14}} + \frac{b_{1015} n_{15}}{\tau_{15}} + \frac{b_{1016} n_{16}}{\tau_{16}} + \beta_{11} \mathrm{n}_{11} + 2c_8 n_9 n_{12} + c_9 n_{12} n_{14} + c_{10} n_{12} n_{14}, \tag{15}$$

$$\mathrm{Tm}^{3+}(^3H_5):\ \frac{\mathrm{d}n_{11}}{\mathrm{d}t} = w_5 n_{Yb11} n_9 + \frac{b_{1114} n_{14}}{\tau_{14}} + \frac{b_{1116} n_{16}}{\tau_{16}} - \beta_{11} n_{11} + \beta_{12} n_{12}, \tag{16}$$

$$\mathrm{Tm}^{3+}(^3H_4):\ \frac{\mathrm{d}n_{12}}{\mathrm{d}t} = -w_7 n_{Yb11} n_{12} + \frac{b_{1214} n_{14}}{\tau_{14}} + \frac{b_{1215} n_{15}}{\tau_{15}} - \frac{n_{12}}{\tau_{12}} - \beta_{12} \mathrm{n}_{12} + \beta_{13} n_{13} + c_{12} n_9 n_{15} - c_8 n_9 n_{12} - c_9 n_{12} n_{14} - c_{10} n_{12} n_{14}, \tag{17}$$

$$\mathrm{Tm}^{3+}(^3F_3/^3F_2):\ \frac{\mathrm{d}n_{13}}{\mathrm{d}t} = w_6 n_{Yb11} n_{10} + \frac{b_{1315} n_{15}}{\tau_{15}} - \frac{n_{13}}{\tau_{13}} - \beta_{13} n_{13} + \beta_{14} n_{14} + c_{12} n_9 n_{15}, \tag{18}$$

$$\mathrm{Tm}^{3+}(^1G_4):\ \frac{\mathrm{d}n_{14}}{\mathrm{d}t} = w_7 n_{Yb11} n_{12} - w_8 n_{Yb11} n_{14} - \frac{n_{14}}{\tau_{14}} - \beta_{14} n_{14} + \beta_{15} n_{15} - c_9 n_{12} n_{14} - c_{10} n_{12} n_{14}, \tag{19}$$

$$\mathrm{Tm}^{3+}(^1D_2):\ \frac{\mathrm{d}n_{15}}{\mathrm{d}t} = w_8 n_{Yb11} n_{14} - w_9 n_{Yb11} n_{15} - \frac{n_{15}}{\tau_{15}} - \beta_{15} n_{15} + \beta_{16} n_{16} + c_9 n_{12} n_{14} + c_{10} n_{12} n_{14} - c_{12} n_9 n_{15}, \tag{20}$$

$$\mathrm{Tm}^{3+}(^1I_6):\ \frac{\mathrm{d}n_{16}}{\mathrm{d}t} = w_9 n_{Yb11} n_{15} - w_{10} n_{16} n_{17} - \frac{n_{16}}{\tau_{16}} - \beta_{16} n_{16}, \tag{21}$$

$$\mathrm{Gd_1}^{3+}(^8S_{7/2}):\ \frac{\mathrm{d}n_{17}}{\mathrm{d}t} = -w_{10}n_{16}n_{17} + w_{11}n_{18}n_{19} + \frac{n_{18}}{\tau_{18}}, \quad (22)$$

$$\mathrm{Gd_1}^{3+}(^6P_{7/2}):\ \frac{\mathrm{d}n_{18}}{\mathrm{d}t} = -w_{11}n_{18}n_{19} + w_{10}n_{16}n_{17} - \frac{n_{18}}{\tau_{18}}, \quad (23)$$

$$\mathrm{Gd_2}^{3+}(^8S_{7/2}):\ \frac{\mathrm{d}n_{19}}{\mathrm{d}t} = -w_{11}n_{18}n_{19} + w_{12}n_{20}n_{21} + \frac{n_{20}}{\tau_{20}}, \quad (24)$$

$$\mathrm{Gd_2}^{3+}(^6P_{7/2}):\ \frac{\mathrm{d}n_{20}}{\mathrm{d}t} = -w_{12}n_{20}n_{21} + w_{11}n_{18}n_{19} - \frac{n_{20}}{\tau_{20}}, \quad (25)$$

$$X^{3+}(\mathrm{ground}):\ \frac{\mathrm{d}n_{21}}{\mathrm{d}t} = -w_{12}n_{20}n_{21} + \frac{n_{22}}{\tau_{22}}, \quad (26)$$

$$X^{3+}(\mathrm{excited}):\ \frac{\mathrm{d}n_{22}}{\mathrm{d}t} = w_{12}n_{20}n_{21} - \frac{n_{22}}{\tau_{22}}. \quad (27)$$

In Eqs. (1)–(27), n_i ($i = 0-8$) denotes the population densities of the $^3H_4$, $^3H_5$, $^3H_6$, $^3F_2$, $^3F_4$, $^1G_4$, $^1D_2$, $^3P_0$, and $^3P_1$ states of Pr^{3+}; n_i ($i = 9-16$) denotes the population densities of the $^3H_6$, $^3F_4$, $^3H_5$, $^3H_4$, $^3F_2/^3F_3$, $^1G_4$, $^1D_2$, and $^1I_6$ states of Tm^{3+}; and n_i ($i = 17-22$) denotes the population densities of the $^8S_{7/2}$, $^6P_{7/2}$, $^8S_{7/2}$, and $^6P_{7/2}$ states of Gd^{3+}, the ground and excited states of X^{3+}, whereas n_{Yb1} and n_{Yb11} denote the population densities of the $^2F_{7/2}$ and $^2F_{5/2}$ states of Yb^{3+}, respectively. β_i ($i = 1, 2, 3, 4, 5, 7, 8$) is the nonradiative decay ratio of the $^3H_5$, $^3H_6$, $^3F_2$, $^3F_4$, $^1G_4$, $^3P_0$, and $^3P_1$ states of Pr^{3+}, respectively. β_i ($i = 11-16$) is the nonradiative decay ratio of the $^3H_5$, $^3H_4$, $^3F_3$, $^1G_4$, $^1D_2$, and $^1I_6$ states of Tm^{3+}, respectively. τ_i ($i = 5, 6, 7, 8$) refers to the radiative lifetime of the $^1G_4$, $^1D_2$, $^3P_0$, and $^3P_1$ states of Pr^{3+}. τ_i ($i = 10, 12, 13, 14, 15, 16$) refers to the radiative lifetime of the $^3F_4$, $^3H_4$, $^3F_3$, $^1G_4$, $^1D_2$, and $^1I_6$ states of Tm^{3+}. τ_i ($i = 18, 22$) refers to the radiative lifetime of the $^6P_{7/2}$ of Gd^{3+} and the excited state of X^{3+}, respectively. τ_{Yb} is the lifetime of the $^2F_{5/2}$ state of Yb^{3+}. b_{ij} ($i > j$) is the branching ratio for the radiative transition from the initial state i to the terminal state j of Pr^{3+} and Tm^{3+}. c_i ($i = 1, 2, 3, 4, 5, 6, 7$) denotes the $Pr^{3+}-Pr^{3+}$ cross-relaxation processes $^3P_0 + {}^3H_4 \rightarrow {}^1G_4 + {}^1G_4$, $^1D_2 + {}^3H_4 \rightarrow {}^3F_4 + {}^1G_4$, $^1G_4 + {}^3H_4 \rightarrow {}^3H_6 + {}^3F_2$, $^3P_0 + {}^3H_4 \rightarrow {}^1D_2 + {}^3H_6$, $^3P_0 + {}^3H_4 \rightarrow {}^3H_6 + {}^1D_2$, $^3P_1 + {}^3H_4 \rightarrow {}^1D_2 + {}^3F_2$, $^1D_2 + {}^3H_4 \rightarrow {}^1G_4 + {}^3F_4$, respectively. c_i ($i = 8, 9, 10, 12$) denotes the $Tm^{3+}-Tm^{3+}$ cross-relaxation processes $^3H_4 + {}^3H_6 \rightarrow {}^3F_4 + {}^3F_4$, $^1D_2 + {}^3F_4 \rightarrow {}^3H_4 + {}^1G_4$, $^1D_2 + {}^3F_4 \rightarrow {}^1G_4 + {}^3H_4$, $^1D_2 + {}^3H_6 \rightarrow {}^3F_2 + {}^3H_4$, respectively. w_i ($i = 1, 2, 3, 4, 5, 6, 7, 8, 9, 10, 11, 12$) is the rate of energy transfer processes $^2F_{5/2}(Yb^{3+}) + {}^3H_4(Pr^{3+}) \rightarrow {}^2F_{7/2}(Yb^{3+}) + {}^1G_4(Pr^{3+})$, $^1D_2(Pr^{3+}) + {}^2F_{7/2}(Yb^{3+}) \rightarrow {}^3F_4(Pr^{3+}) + {}^2F_{5/2}(Yb^{3+})$, $^3P_0(Pr^{3+}) + {}^2F_{7/2}(Yb^{3+}) \rightarrow {}^1G_4(Pr^{3+}) + {}^2F_{5/2}(Yb^{3+})$, $^2F_{5/2}(Yb^{3+}) + {}^2F_{7/2}(Yb^{3+}) \rightarrow {}^2F_{5/2}(Yb^{3+}) + {}^2F_{7/2}(Yb^{3+})$, $^2F_{5/2}(Yb^{3+}) + {}^2F_{7/2}(Yb^{3+}) \rightarrow {}^3H_6(Tm^{3+}) + {}^3H_5(Tm^{3+})$, $^2F_{5/2}(Yb^{3+}) + {}^2F_{7/2}(Yb^{3+}) \rightarrow {}^3H_5(Tm^{3+}) + {}^3F_2(Tm^{3+})$, $^2F_{5/2}(Yb^{3+}) + {}^2F_{7/2}(Yb^{3+}) \rightarrow {}^3H_4(Tm^{3+}) + {}^1G_4(Tm^{3+})$, $^2F_{5/2}(Yb^{3+}) + {}^2F_{7/2}(Yb^{3+}) \rightarrow {}^1G_4(Tm^{3+}) + {}^1D_2(Tm^{3+})$, $^2F_{5/2}(Yb^{3+}) + {}^2F_{7/2}(Yb^{3+}) \rightarrow {}^1D_2(Tm^{3+}) + {}^1I_6(Tm^{3+})$, $^3H_6(Tm^{3+}) + {}^1I_6(Tm^{3+}) \rightarrow {}^8S_{7/2}(Gd^{3+}) + {}^6P_{7/2}(Gd^{3+})$, $^8S_{7/2}(Gd^{3+}) + {}^6P_{7/2}(Gd^{3+}) \rightarrow \mathrm{excited}(X^{3+}) + \mathrm{ground}(X^{3+})$, respectively. w'_i ($i = 1, 2, 3$) is the rate of back-energy transfer processes $^1G_4(Pr^{3+}) + {}^2F_{7/2}(Yb^{3+}) \rightarrow {}^3H_4(Pr^{3+}) + {}^2F_{5/2}(Yb^{3+})$, $^2F_{5/2}(Yb^{3+}) + {}^3F_4(Pr^{3+}) \rightarrow {}^2F_{7/2}(Yb^{3+}) + {}^1D_2(Pr^{3+})$, $^2F_{7/2}(Yb^{3+}) + {}^1G_4(Pr^{3+}) \rightarrow {}^3P_0(Pr^{3+}) + {}^2F_{5/2}(Yb^{3+})$, respectively. I_{852} is the excitation intensity of the 852 nm laser beam. $\hbar$ is the Planck constant, and υ is the frequency of the 852 nm laser light. The difference in the wavenumber between 852 nm and $^2F_{5/2}$ (Yb^{3+}) is 1489 cm^{-1} and between 852 nm and $^1G_4$ (Pr^{3+}) is 1884 cm^{-1}, indicating very weak GSA. σ_0, σ_5, and σ_{Yb0} are the cross-sections of absorption processes $^3H_4 \rightarrow {}^1G_4(Pr^{3+})$, $^1G_4 \rightarrow {}^3P_1(Pr^{3+})$, and $^2F_{7/2} \rightarrow {}^2F_{5/2}(Yb^{3+})$ under excitation of the 852 nm laser. A numerical solution can be obtained by solving these rate equations with a computer. The parameters (Table S1 in the Supplementary Material) were varied within a reasonable range to investigate the photon avalanche process.

5 Appendix B: Optical Setup and Measurements

5.1 Optical Setup for Laser Power-Dependent Emission Spectroscopy

A laboratory-made optical system was built to measure the emission spectra for power dependence analysis. The optical measurement setup was based on a conventional microscope (IX81, Olympus), as shown in Fig. S5 of Supplementary Material. The 852 nm CW excitation beam was provided by a tunable Ti:sapphire laser (Mira 900, Coherent, Santa Clara, California, United States). A band-pass filter (FF01-850/10-25, Semrock) was used to clean the laser spectrum. To optimize the beam profile, the laser was coupled to a single-mode fiber using a FiberPort coupler (PAF-X-11-PC-B, Thorlabs, Newton, New Jersey, United States). Then, the laser was collimated by a fiber collimator (F280APC-850, Thorlabs) and directed into the microscope. The beam was reflected by a 690 nm short-pass dichroic mirror (T690spxxf-UF1, Chroma, Bellows Falls, Vermont, United States) and focused on the sample using an oil immersion objective (UPlanXApo, 100×/1.45, Olympus, Japan).

As shown in Fig. S5, the photon avalanche upconversion emissions were collected by the objectives. The visible emission (400 to 700 nm) passed through the short-pass dichroic mirror and was filtered by two short-pass filters (F3, FF02-694/SP-25, Semrock; F4, FF01-842/SP-25, Semrock, Rochester, New York, United States). Then, the emission light was coupled into a multimode fiber, which guided the signal light to a visible spectrometer (QE65000, spectral range of 350 to 1000 nm, Ocean Optics, Orlando, Florida, United States). A pair of half-wave plates and polarization beam splitters were placed in the optical path to adjust the excitation power, which was recorded by a power meter using an uncoated pellicle beam splitter to reflect about 5% of the laser beam. The diameter of the laser focus spot was defined as the full width at $1/e^2$ of maximum, and the laser intensity of PA excitation was calculated by dividing the power by the area of the laser spot.

5.2 Optical Setup for cMPA Super-Resolution Microscopy

As illustrated in Fig. 5(a), the optical system for super-resolution imaging was based on a galvanometer mirror multiphoton laser scanning microscope. The 852 nm CW laser was filtered with a band-pass filter (FF01-850/10-25, Semrock). (The 852 nm laser beam could also be provided by commercially available

diode lasers, for example, L852H1 or FPL852P from Thorlabs.) Then, the laser was coupled into a single-mode fiber, which functions as a spatial filter to optimize the beam profile. The collimated laser beam was directed into the imaging system. Non-descanned detectors in combination with galvanometer scanning mirrors were used to perform laser scanning microscopic imaging. A PMT was employed for the imaging studies, and two short-pass filters (F2, FF02-694/SP-25, Semrock; F3, FF01-665/SP-25, Semrock) were used to further filter the signal for imaging.

Disclosures

The authors declare no conflicts of interest.

Code and Data Availability

The data and code supporting this study are available from the corresponding author upon request.

Supplementary Material

Sample preparation and characterizations, theoretical simulations for the cMPA nano-engine, and any other supplementary figures are provided in the Supplementary Material.

Acknowledgments

This work was supported by the National Natural Science Foundation of China (Grant Nos. 62122028 and 62335008), Guangdong Basic and Applied Basic Research Foundation (Grant Nos. 2023B1515040018 and 2018B030306015), National Key Research and Development Program of China (Grant No. 2023YFF0722600), and Scientific Research Cultivation Fund for Young Faculty of South China Normal University (Grant Nos. 23KJ01 and 22KJ30).

References

1. H. Zhang et al., "Photon-avalanche upconversion of Ho^{3+} in $NaYF_4$ and enhancement of violet, blue and green emissions induced by sensitization of Tm^{3+}," *Mater. Sci. Eng. B* **176**, 256–259 (2011).
2. C. Lee et al., "Giant nonlinear optical responses from photon-avalanching nanoparticles," *Nature* **589**, 230–235 (2021).
3. Y. Liang et al., "Migrating photon avalanche in different emitters at the nanoscale enables 46th-order optical nonlinearity," *Nat. Nanotechnol.* **17**, 524–530 (2022).
4. A. Fernandez-Bravo et al., "Continuous-wave upconverting nanoparticle microlasers," *Nat. Nanotechnol.* **13**, 572–577 (2018).
5. K. Koshelev et al., "Subwavelength dielectric resonators for non-linear nanophotonics," *Science* **367**, 288–292 (2020).
6. A. Bednarkiewicz et al., "Photon avalanche in lanthanide doped nanoparticles for biomedical applications: super-resolution imaging," *Nanoscale Horiz.* **4**, 881–889 (2019).
7. W. Wang et al., "Dual-modulation difference stimulated emission depletion microscopy to suppress the background signal," *Adv. Photonics* **4**, 046001 (2022).
8. A. Bednarkiewicz, E. M. Chan, and K. Prorok, "Enhancing FRET biosensing beyond 10 nm with photon avalanche nanoparticles," *Nanoscale Adv.* **2**, 4863–4872 (2020).
9. L. Marciniak, A. Bednarkiewicz, and K. Elzbieciak, "NIR–NIR photon avalanche based luminescent thermometry with Nd^{3+} doped nanoparticles," *J. Mater. Chem. C* **6**, 7568–7575 (2018).
10. C. Bradac et al., "Room-temperature spontaneous superradiance from single diamond nanocrystals," *Nat. Commun.* **8**, 1205 (2017).
11. F. Wang et al., "Tuning upconversion through energy migration in core–shell nanoparticles," *Nat. Mater.* **10**, 968–973 (2011).
12. E. S. Levy et al., "Energy-looping nanoparticles: harnessing excited-state absorption for deep-tissue imaging," *ACS Nano* **10**, 8423–8433 (2016).
13. M.-F. Joubert, "Photon avalanche upconversion in rare earth laser materials," *Opt. Mater.* **11**, 181–203 (1999).
14. S. Kück et al., "Avalanche up-conversion processes in Pr, Yb-doped materials," *J. Alloys Compd.* **300–301**, 65–70 (2000).
15. E. Osiac et al., "Spectroscopic characterisation of the upconversion avalanche mechanism in Pr^{3+}, $Yb^{3+}:BaY_2F_8$," *Opt. Mater.* **24**, 537–545 (2003).
16. H. Scheife et al., "Advances in up-conversion lasers based on Er^{3+} and Pr^{3+}," *Opt. Mater.* **26**, 365–374 (2004).
17. P. Goldner et al., "Orange avalanche upconversion for high-resolution laser spectroscopy," *EPJ Appl. Phys.* **37**, 161–168 (2007).
18. L. Li et al., "A theoretical study of intrinsic optical bistability dynamics in Tm^{3+}/Yb^{3+} codoped systems with an upconversion avalanche mechanism," *J. Opt. A: Pure Appl. Opt.* **11**, 105203 (2009).
19. K. Mishra, Y. Dwivedi, and S. B. Rai, "Observation of avalanche upconversion emission in $Pr:Y_2O_3$ nanocrystals on excitation with 532 nm radiation," *Appl. Phys. B* **106**, 101–105 (2012).
20. M. Wermuth and H. U. Güdel, "Photon avalanche in $Cs_2ZrBr_6:Os^{4+}$," *J. Am. Chem. Soc.* **121**, 10102–10111 (1999).
21. D. Peng et al., "Lanthanide-doped energy cascade nanoparticles: full spectrum emission by single wavelength excitation," *Chem. Mater.* **27**, 3115–3120 (2015).
22. A. Skripka et al., "A generalized approach to photon avalanche upconversion in luminescent nanocrystals," *Nano Lett.* **23**, 7100–7106 (2023).
23. Q. Zhan et al., "Achieving high-efficiency emission depletion nanoscopy by employing cross relaxation in upconversion nanoparticles," *Nat. Commun.* **8**, 1058 (2017).
24. N. J. J. Johnson et al., "Self-focusing by Ostwald ripening: a strategy for layer-by-layer epitaxial growth on upconverting nanocrystals," *J. Am. Chem. Soc.* **134**, 11068–11071 (2012).
25. F. Wang, R. Deng, and X. Liu, "Preparation of core-shell $NaGdF_4$ nanoparticles doped with luminescent lanthanide ions to be used as upconversion-based probes," *Nat. Protoc.* **9**, 1634–1644 (2014).
26. X. Li et al., "Energy migration upconversion in manganese (II)-doped nanoparticles," *Angew. Chem. Int. Ed.* **54**, 13312–13317 (2015).
27. Q. Zou et al., "Cooperative and non-cooperative sensitization upconversion in lanthanide-doped $LiYbF_4$ nanoparticles," *Nanoscale* **9**, 6521–6528 (2017).
28. D. Dong et al., "Super-resolution fluorescence-assisted diffraction computational tomography reveals the three-dimensional landscape of the cellular organelle interactome," *Light Sci. Appl.* **9**, 11 (2020).
29. G. Huang et al., "Upconversion nanoparticles for super-resolution quantification of single small extracellular vesicles," *eLight* **2**, 20 (2022).
30. C. Chen and D. Jin, "Giant nonlinearity in upconversion nanoparticles," *Nat. Photonics* **16**, 553–554 (2022).
31. X. Hao and C. Kuang, "Towards extremely high-order optical nonlinearity at the nanoscale," *Adv. Photonics* **4**, 020501 (2022).
32. S. Wen et al., "Future and challenges for hybrid upconversion nanosystems," *Nat. Photonics* **13**, 828–838 (2019).
33. S. Lamon et al., "Nanoscale optical writing through upconversion resonance energy transfer," *Sci. Adv.* **7**, eabe2209 (2021).
34. M. Gu, X. Li, and Y. Cao, "Optical storage arrays: a perspective for future big data storage," *Light Sci. Appl.* **3**, e177 (2014).
35. S. N. Sanders et al., "Triplet fusion upconversion nanocapsules for volumetric 3D printing," *Nature* **604**, 474–478 (2022).
36. X. Chen et al., "Photon upconversion in core-shell nanoparticles," *Chem. Soc. Rev.* **44**, 1318–1330 (2015).

37. G. Ajithkumar et al., "Judd-Ofelt intensity parameters and laser analysis of Pr^{3+} doped phosphate glasses sensitized by Mn^{2+} ions," *J. Non-Cryst. Solids* **275**, 93–106 (2000).
38. J. Dong et al., "Dependence of the Yb^{3+} emission cross section and lifetime on temperature and concentration in yttrium aluminum garnet," *J. Opt. Soc. Am. B* **20**, 1975–1979 (2003).
39. P. Villanueva-Delgado, D. Biner, and K. W. Kramer, "Judd-Ofelt analysis of beta-$NaGdF_4:Yb^{3+}$, Tm^{3+} and beta-$NaGdF_4:Er^{3+}$ single crystals," *J. Lumin.* **189**, 84–90 (2017).
40. B. M. Walsh and N. P. Barnes, "Comparison of Tm:ZBLAN and Tm:silica fiber lasers; spectroscopy and tunable pulsed laser operation around 1.9 μm," *Appl. Phys. B* **78**, 325–333 (2004).
41. Q. Su et al., "The effect of surface coating on energy migration-mediated upconversion," *J. Am. Chem. Soc.* **134**(51), 20849–20857 (2012).
42. X. Ping and T. R. Gosnell, "Efficient sensitisation of praesodymium 1.31 μm fluorescence by optically pumped ytterbium ions in ZBLAN glass," *Electron. Lett.* **31**, 191–192 (1995).
43. L. D. Merkle et al., "Spectroscopy and laser operation of Pr, $Mg:SrAl_{12}O_{19}$," *J. Appl. Phys.* **79**, 1849–1856 (1996).
44. C. K. Jayasankar and V. Kumar, "Judd-Ofelt intensity analysis and spectral studies of Pr(III) ions in alkali zinc borosulphate glasses," *Mater. Chem. Phys.* **46**, 84–91 (1996).

Hui Wu received her master's degree in materials physics and chemistry from South China Normal University in 2023. Her research interests include advanced optical materials and near-infrared upconversion fluorescence.

Binxiong Pan received his BE degree in information engineering from South China Normal University (SCNU) in 2020. He is currently pursuing his PhD in optics at SCNU. His research interests include super-resolution fluorescence microscopy and near-infrared upconversion fluorescence.

Qi Zhao received her master's degree in polymeric chemistry and physics from South China Normal University in 2023. Her research interests include advanced optical materials and near-infrared upconversion fluorescence.

Rui Pu received his PhD in optics from South China Normal University in 2023. He is currently a postdoctoral researcher at the South China Academy of Advanced Optoelectronics, South China Normal University. His research interests include super-resolution fluorescence microscopy and lanthanide luminescence materials.

Zewei Luo received his PhD in optics from South China Normal University in 2024. He is currently a postdoctoral researcher at the College of Biophotonics, South China Normal University. His research primarily focuses on advancing super-resolution microscopy and *in situ* FRET (Förster resonance energy transfer) microscopy.

Jing Huang received her PhD in biophotonics from Jena University, supervised by Prof. Dr. Jürgen Popp in 2020. Later, she continued her academic career as a postdoctoral researcher at Fudan University from 2020 to 2022, mainly focusing on biophotonics and translational biophotonics. Currently, she is a research associate at South China Normal University, with the research interests of biophotonics and translational biophotonics.

Wei Wei is currently an associate professor at the College of Biophotonics, South China Normal University (China). He obtained his BE degree from the Beijing University of Chemical Technology (China) in 2010 and earned his PhD from Nanyang Technological University (Singapore). His research interest focuses on the fundamental study and application of lanthanide-based luminescent nanomaterials.

Tongsheng Chen received his PhD in biomedical engineering from Huazhong University of Science and Technology. He is the director of the College of Biophotonics at South China Normal University. He developed the world's first intelligent quantitative FRET imaging analysis system. His research focuses on biophotonics, the advancement of FRET (fluorescence resonance energy transfer) microscopy, and cell biology, with a particular emphasis on the molecular mechanisms of cellular signal transduction.

Qiuqiang Zhan is currently a full professor of optics at South China Normal University, China. He received his BS degree in optics from Shandong University and performed his doctoral research in the Optical Engineering Department at Zhejiang University. He had visiting research in Lund University, Sweden, and the Chinese University of Hong Kong. His research interests mainly include near-infrared upconversion fluorescence, super-resolution fluorescence microscopy, and bio-nanophotonics.

Biographies of the other authors are not available.